Applied Catalysis B: Environment and Energy 403 (2027) 127622

Contents lists available at ScienceDirect

Applied Catalysis B: Environment and Energy

journal homepage: www.elsevier.com/locate/apcatb

Rational N,O co-coordination of Fe-N_2O_2 single atoms modulates the electronic structure to facilitate $^1O_2$ generation

Chengyu Hu [a,b,1], Qian Yao [a,1], Liangzhong Li [a,*], Juhai Liu [a,b], Chenyu Yang [a], Xiang He [a], Lida Yang [a,c], Yingxin Yu [b], Rui Shan [a], Sihui Zhan [d], Haoran Yuan [a]

[a] Guangdong Provincial Key Laboratory of High-Quality Recycling of End-of-Life New Energy Devices, Guangzhou Institute of Energy Conversion, Chinese Academy of Sciences (CAS), Guangdong, 510640, PR China

[b] Guangdong-Hong Kong-Macao Joint Laboratory for Contaminants Exposure and Health, Guangdong Key Laboratory of Environmental Catalysis and Health Risk Control, Institute of Environmental Health and Pollution Control, School of Environmental Science and Engineering, Guangdong University of Technology, Guangzhou, 510006, PR China

[c] School of Energy Science and Engineering, University of Science and Technology of China, Hefei, Anhui, 230026, PR China

[d] School of Environmental Science and Engineering, Tianjin University, Tianjin, 300350, PR China

ARTICLE INFO

Keywords:
Single-atom catalyst
Peroxymonosulfate activation
Phenolic pollutants
Singlet oxygen
Coordination engineering

ABSTRACT

Selective generation of reactive oxygen species (ROS) remains a major challenge in single-atom-catalyst-based advanced oxidation systems, especially in complex water matrices. Herein, a Schiff-base ligand was used to regulate the local N,O coordination environment of Fe sites, yielding an N,O-coordinated carbon-supported Fe single-atom catalyst denoted as Fe-N_2O_2 based on the proposed idealized coordination model. Compared with Fe-N_4, Fe-N_2O_2 exhibited a higher Fe oxidation state, improved electrical conductivity, and enhanced phenol (PN) adsorption (22.3% vs 5.62%). The Fe-N_2O_2/PMS system also showed enhanced involvement of $^1O_2$ during PMS activation. As a result, PN, a representative electron-rich phenolic pollutant, was completely removed within 5 min. The apparent rate constant reached 2.51 min^{-1}, and total organic carbon removal reached 73.1% within 30 min. Theoretical calculations revealed that N,O co-coordination reduced Fe charge density and lowered the Gibbs free energy change (ΔG) of O* formation, facilitating PMS activation and $^1O_2$ generation. The favorable cycling stability and continuous-flow performance (>94.9% PN removal within 36 h) highlight the practical potential of the Fe-N_2O_2/PAN membrane. This work demonstrates that Schiff-base-defined N,O coordination is a viable strategy for regulating ROS evolution in PMS-based catalytic oxidation systems.

1. Introduction

Phenolic pollutants and their derivatives pose persistent ecological and health risks even at trace concentrations, necessitating efficient and selective degradation technologies [1–4]. Peroxymonosulfate (PMS)-mediated heterogeneous advanced oxidation processes (AOPs) have been widely investigated as promising technologies for degrading refractory organic contaminants [5–7]. Compared with hydrogen peroxide (H_2O_2) and peroxydisulfate (PDS, $S_2O_8^{2-}$), PMS is more readily activated [8]. It can generate both radical species, including hydroxyl radical (·OH), sulfate radical ($SO_4^{\cdot-}$), and superoxide radical ($O_2^{\cdot-}$), and non-radical species ($^1O_2$ or electron-transfer complexes) [9,10]. Singlet oxygen ($^1O_2$) preferentially attacks electron-rich centers in phenolic compounds and can facilitate their subsequent oxidative transformation [11,12]. Phenol (PN) and bisphenol A (BPA), which contain π-electron-rich aromatic rings, are therefore particularly susceptible to $^1O_2$ attack. Luo et al. [13] reported that selective activation of PMS by nitrogen-doped graphitic carbon generated $^1O_2$ and enabled efficient BPA degradation. Moreover, $^1O_2$ is less susceptible than conventional radicals to quenching by natural organic matter (NOM), HCO_3^-, and Cl^-. Therefore, $^1O_2$-involved oxidation can retain high reactivity in complex water matrices [14,15]. Thus, developing catalysts that steer PMS activation toward a $^1O_2$-involved non-radical oxidation pathway remains highly desirable.

Among the catalysts explored for PMS activation, single-atom catalysts (SACs) have attracted considerable attention because of their

* Corresponding author.
E-mail address: lilz@ms.giec.ac.cn (L. Li).
[1] These authors contributed equally to this manuscript.

https://doi.org/10.1016/j.apcatb.2026.127622
Received 30 July 2026; Received in revised form 7 October 2026; Accepted 8 October 2026
Available online 8 October 2026
0926-3373/© 2026 Elsevier B.V. All rights are reserved, including those for text and data mining, AI training, and similar technologies.

maximized atom utilization, tunable coordination environments, and atomically dispersed active sites [16,17]. Coordination engineering can regulate the charge density of metal centers and thereby alter PMS activation and ROS generation [18]. Heteroatom coordination is particularly effective because changes in local bonding and structural symmetry can induce electronic polarization and d-orbital redistribution [19,20]. Increasing evidence has revealed a close relationship between the electronic state of metal centers and $^1O_2$ generation [21]. Appropriate electron deficiency or enrichment can regulate PMS adsorption and O–O bond cleavage, thereby affecting the competition between radical and non-radical pathways [22,23].

For example, Long et al. [24] introduced electron-deficient boron (B) atoms to construct a six-coordinate Fe-N_2B_4 structure, which reduced the charge density of the Fe center and increased $^1O_2$ selectivity from 64.6% for Fe-N_4 to 98.7%. Similarly, Zeng et al. [18] demonstrated that O coordination at Fe-N_3O_1 sites regulated PMS activation and enabled antibiotic degradation through the synergistic involvement of $^1O_2$ and Fe(IV)=O. Zhang et al. [25] further showed that second-shell O coordination could modulate the electronic structure and stability of Fe single-atom sites and enhance Fe(IV)=O-mediated oxidation. These studies establish the importance of heteroatom doping in regulating the electronic properties of metal centers, but the relationship between first-shell coordination, metal-center electronic redistribution, and interfacial PMS activation remains less explored.

Schiff bases contain imine and adjacent oxygen-containing groups that can coordinate with metal ions through N,O chelation [26]. The resulting M-N_2O_2 centers provide a well-defined coordination platform for regulating the electronic structure of metal sites during PMS activation [27,28]. Among transition metals, Fe was selected because of its variable valence states and strong affinity. Structurally related $Fe_1N_2O_2$ sites have also been reported for electrochemical CO_2 reduction [29], confirming the feasibility of N,O co-coordination around isolated Fe sites. Herein, we employed Schiff-base pre-coordination to regulate the local N,O coordination environment of isolated Fe sites. Fe-N_2O_2 exhibited distinct electronic and catalytic behavior compared with Fe-N_4. N,O coordination was associated with enhanced PMS activation and a greater involvement of $^1O_2$ during PN degradation. Density functional theory (DFT) calculations further showed that N,O co-coordination redistributed the electron density around the Fe center. This electronic redistribution facilitated interfacial charge transfer and lowered the Gibbs free energy change (ΔG) of O* formation during PMS activation. Recycling and continuous-flow tests further evaluated the stability and reusability of Fe-N_2O_2. Overall, this work establishes a structure–electronic property–reactivity relationship between N,O coordination, Fe electronic redistribution, and PMS activation, providing guidance for the rational design of coordination-engineered single-atom catalysts.

2. Materials and methods

2.1. Material preparation

An N,O-coordinated Fe single-atom catalyst, denoted as Fe-N_2O_2 based on the proposed Salophen-derived idealized coordination model, was prepared using a hard-template-assisted synthesis method. First, the tetradentate N_2O_2-type Schiff base ligand (Salophen ligand) was prepared via a hydrothermal method according to previous reports [30,31]. Briefly, *o*-phenylenediamine was reacted with salicylaldehyde under heating, followed by vacuum filtration and three methanol washes. The resulting ligand was then dried overnight to obtain the Salophen ligand.

For the synthesis of the Fe-N_2O_2 single-atom catalyst, 6 mmol of iron (II) acetate was dissolved in 200 mL of anhydrous ethanol, followed by the addition of 6 mmol of Salophen ligand. After stirring for 5 min, 12.8 g of MgO was added, and the mixture was sonicated for 10 min. The mixed solution was then heated and stirred in an 80 °C oil bath for 12 h, followed by concentration using a rotary evaporator at 65 °C. The resulting solid was dried overnight at 60 °C, ground, sieved, and calcined in a tube furnace. The sample was heated to 600 °C under a N_2 atmosphere at a ramping rate of 2 °C min^{-1} and then held at this temperature for 2 h. After calcination, the sample was ground, sieved, and acid-washed with 1 mol L^{-1} H_2SO_4 at 60 °C for 8 h, followed by filtration, washing, and drying to obtain Fe-N_2O_2. As a control sample, Fe-N_4 was synthesized by replacing the Salophen ligand with *o*-phenanthroline under otherwise identical conditions. A metal-free N_2O_2 catalyst was also prepared using the same procedure without the addition of iron (II) acetate.

Additional experimental details, including reagent information, instrument specifications, and analysis methods, are provided in the Supporting Information.

2.2. Experimental procedure

The catalytic activity of the Fe-N_2O_2 single-atom catalyst was evaluated in a 50 mL flask containing PN solution (50 mL, 10 mg L^{-1}), PMS (1.0 mM), and catalyst (0.15 g L^{-1}). The solution pH was adjusted using HCl (0.1 M) or NaOH (0.1 M). Before initiating the reaction, the catalyst was added to the PN solution and stirred for 5 min to establish adsorption-desorption equilibrium. The Fenton-like reaction was then initiated by adding PMS solution. At predetermined time intervals, 0.5 mL aliquots were withdrawn, filtered through a 0.22 μm membrane, and analyzed for residual PN concentration.

The concentrations of organic pollutants were determined by high-performance liquid chromatography (HPLC, Agilent 1260 Infinity II, USA) equipped with a C18 reverse-phase column (Agilent SB-C18, 5 μm, 4.6 mm × 250 mm). Detailed detection conditions for PN and the other target compounds are listed in Table S1. The reaction kinetics were evaluated using a pseudo-first-order (PFO) kinetic model, and the apparent rate constant (k_{obs}) was used to assess removal performance (Text S3). In addition, the effects of inorganic anions and cations, natural organic matter, and different water matrices on PN removal were systematically investigated. ROS were identified by quenching experiments and electron paramagnetic resonance (EPR) spectroscopy, while the detailed procedure for estimating the apparent relative ROS involvement is provided in Text S5. Unless otherwise specified, all experiments were independently performed in triplicate, and the reported values represent the mean results.

2.3. Computational methodology

The DFT computations were performed with Gaussian 16 using the B3LYP functional and the 6–311 + + G(d,p) basis set [32]. Geometries of reactants and products were optimized, and frequency calculations were performed to confirm stationary points and obtain Gibbs free energies. PMS adsorption at different oxygen sites on Fe-N_2O_2 and Fe-N_4 was compared, and the most favorable adsorption configurations were used to construct free-energy profiles and identify the key activation-related Gibbs free-energy changes (ΔG). Energy values are consistently expressed in electron volts (eV) throughout this study.

3. Results and discussion

3.1. Synthesis and structural characterization

An Fe-based single-atom catalyst featuring N,O co-coordinated Fe sites was synthesized via a Salophen-ligand-assisted sacrificial-template route (Fig. 1a). The Salophen ligand serves as a pre-coordination platform, where the N,O donor atoms interact with Fe species and direct the formation of atomically dispersed Fe-N_2O_2 coordination sites during pyrolysis. Scanning electron microscopy (SEM) images demonstrated that Fe-N_2O_2 contained a higher density of nanopores than N_2O_2 and Fe-N_4 (Fig. S1 and S2). This morphology suggests that Fe incorporation and coordination-environment modulation influenced pore formation. The

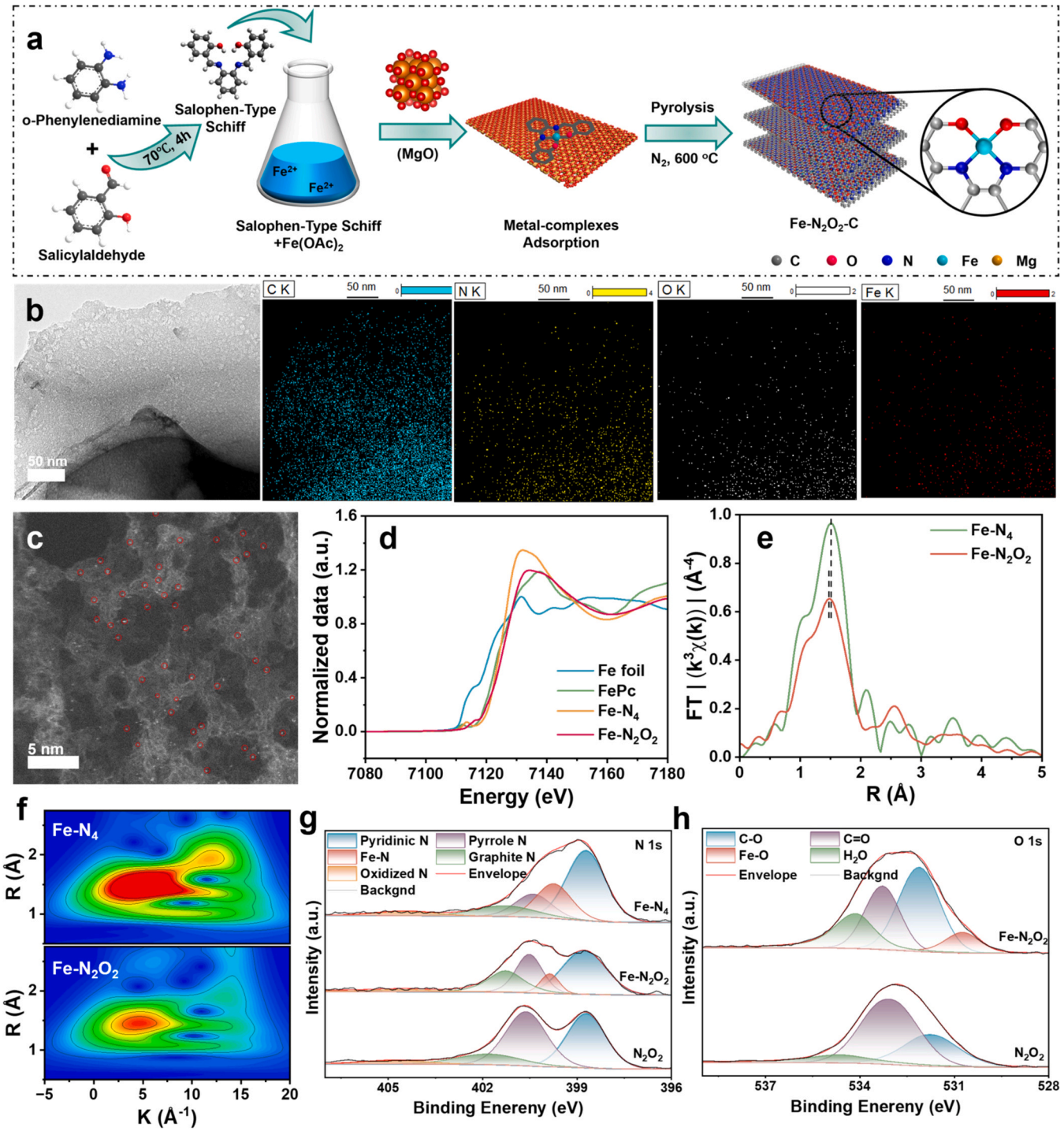


Fig. 1. Morphology characterization. (a) Schematic diagram of the preparation route of Fe-N_2O_2; (b) TEM image and EDS mapping images of Fe-N_2O_2; (c) aberration-corrected HAADF-STEM image; (d) Fe K-edge XANES spectra of Fe foil and various Fe-based materials after normalization; (e) FT-EXAFS spectra at Fe K-edge of Fe-N_4, Fe-N_2O_2, and references in R-space; (f) WT analysis of the Fe K-edge EXAFS spectra of the Fe-N_4 (top) and Fe-N_2O_2 (bottom); (g) N 1 s and (h) O 1 s XPS spectra.

abundant nanopores may also expose more catalytically accessible sites [25]. X-ray diffraction (XRD) patterns of all three samples showed two characteristic peaks of graphitic carbon (Fig. S3). These peaks corresponded to the (002) and (100) planes [33]. No diffraction peaks from crystalline iron or iron oxides were detected. Consistently, transmission electron microscopy (TEM) images of Fe-N_2O_2 and Fe-N_4 (Fig. 1b and Fig. S4) revealed no obvious nanoparticles or cluster aggregates. EDS elemental mapping revealed uniform spatial distributions of Fe, C, N, and O throughout the Fe-N_2O_2 framework (Fig. 1b), supporting the homogeneous dispersion of these elements in the catalyst. Inductively coupled plasma mass spectrometry (ICP-MS) analysis showed that the Fe contents in Fe-N_2O_2 and Fe-N_4 were 2.01 wt% and 6.26 wt%, respectively, indicating a substantial difference in Fe loading between the two catalysts. Furthermore, aberration-corrected high-angle annular dark-field scanning transmission electron microscopy (AC-HAADF-STEM) images displayed isolated bright spots in both Fe-N_2O_2 and Fe-N_4 (Fig. 1c and Fig. S5), confirming that the Salophen ligand and phenanthroline effectively anchored Fe atoms at defect sites [34]. These characterizations collectively provide strong evidence for the formation of single Fe sites in Fe-N_2O_2 and Fe-N_4.

Additionally, Fourier-transform infrared (FT-IR) analysis of Fe-N_4, Fe-N_2O_2, and N_2O_2 (Fig. S6) revealed two absorption bands centered at approximately 1364 and 1595 cm^{-1}, which were assigned to C-C/C-O and C-C/C-N vibrations, respectively. The band at 2830 cm^{-1} was attributed to C-H bond vibrations, indicating that the three materials possessed similar carbon skeletons [35]. However, Raman spectroscopy revealed clear differences in the I_D/I_G ratios of the three materials (Fig. S7). The signal centered at approximately 1352 cm^{-1} (D band) is associated with defect-induced disorder, whereas the band at approximately 1590 cm^{-1} (G band) corresponds to the graphitized sp^2-hybridized carbon framework [36]. Fe-N_4 exhibited a relatively low I_D/I_G value of 1.09, while N_2O_2 showed the highest value of 1.23, exceeding that of Fe-N_2O_2 (1.16). These results indicate that abundant defects were initially present on the ligand-derived surface, which favored the anchoring of Fe atoms, whereas the residual defects retained in Fe-N_2O_2 after Fe incorporation remained sufficient to promote the adsorption and activation of pollutants and oxidants [37]. Consistently, Brunauer-Emmett-Teller (BET) analysis showed that N_2O_2 and Fe-N_2O_2 possessed high specific surface areas of 698.9 and 665.4 $m^2\ g^{-1}$, respectively, with pore sizes mainly distributed within 0–10 nm (Fig. S8 and Table S2). By contrast, Fe-N_4 exhibited a lower specific surface area of 610.1 $m^2\ g^{-1}$ and a broader pore-size distribution of 0–20 nm (Fig. S9). The higher surface area of metal-free N_2O_2 indicates that the porous structure is primarily associated with the Salophen/template-derived framework rather than Fe coordination itself. The porous structure may facilitate pollutant diffusion, PMS transport, and accessibility of Fe active sites. Therefore, although the differences in surface area and pore structure may contribute to the observed catalytic behavior, they cannot be solely attributed to N,O coordination [25].

The local coordination environment and electronic configuration of the Fe-N_2O_2 and Fe-N_4 catalysts were systematically analyzed by X-ray absorption fine structure (XAFS). As shown in Fig. 1d, the Fe K-edge X-ray absorption near-edge structure (XANES) spectra of both catalysts exhibited attenuated white-line features and weak oscillations, which are typical characteristics of atomically dispersed Fe species [38]. Compared with Fe-N_4, the absorption edge of Fe-N_2O_2 shifted to higher energy, indicating a higher oxidation state of the Fe center. This result suggests that N,O co-coordination induced substantial electronic redistribution around Fe and thereby modified its local coordination environment. Further structural information was obtained from the Fourier-transformed k^3-weighted extended XAFS (FT-EXAFS) spectra. As shown in Fig. 1e, the main peaks of Fe-N_4 and Fe-N_2O_2 appeared at 1.51 and 1.47 Å, respectively, and were attributed to scattering interactions between isolated Fe atoms and neighboring light atoms, including N, O, and C. The first-shell peak of Fe-N_2O_2 shifted to a lower R value. This shift suggests that O atoms were incorporated into the first coordination shell. The higher electronegativity of oxygen generally results in a shorter Fe-O bond than the Fe-N bond [39]. By comparison, the main peak of Fe-N_4 at approximately 1.53 Å was primarily assigned to Fe-N coordination (Fig. S10) [40]. In addition, no Fe-Fe scattering path was observed at 2.17 Å, in clear contrast to Fe foil, confirming the atomically dispersed nature of Fe in both catalysts.

This conclusion was further supported by wavelet transform extended XAFS (WT-EXAFS) analysis. The maximum intensity of Fe-N_4 appeared at 6.1 $Å^{-1}$, close to the Fe-N signal of FePc (6.3 $Å^{-1}$) and far from the Fe-O signal of FeO (4.89 $Å^{-1}$), whereas Fe-N_2O_2 showed a distinct leftward shift to 4.65 $Å^{-1}$ (Fig. 1f and Fig. S11) [24]. These results support that atomically dispersed Fe sites were embedded within the sp^2-hybridized carbon matrix and that O coordination played a regulatory role in tailoring the Fe microenvironment. Quantitative least-squares fitting of the FT-EXAFS spectra was further performed to examine the first-shell coordination (Table S3). Fe-N_4 exhibited a four-coordinate Fe-N environment, whereas the fitted Fe-N and Fe-O coordination numbers for Fe-N_2O_2 were 2.6 ± 0.2 and 2.5 ± 0.5, respectively. The corresponding Fe-N and Fe-O bond lengths were 2.04 $\pm$ 0.03 and 1.87 $\pm$ 0.03 Å. The near-unity N,O ratio supports the coexistence of N and O in the local coordination environment of Fe. However, the apparent total coordination number of approximately 5.1 deviates from the ideal four-coordinate Fe-N_2O_2 model, indicating that an exact 2 N + 2 O configuration cannot be assigned from EXAFS alone. This deviation may reflect ensemble averaging, local structural heterogeneity, mixed N,O coordination configurations, or contributions from additional O-containing ligands or adsorbates [29]. Overall, combined AC-HAADF-STEM, XAFS, XANES, and XPS results support isolated Fe atoms with N,O co-coordination.

As depicted in Fig. S14 and Table S4, X-ray photoelectron spectroscopy (XPS) was further employed to analyze the near-surface elemental composition and chemical states of Fe-N_4, Fe-N_2O_2, and N_2O_2. The C 1 s XPS profile (Fig. S15a) exhibited three deconvoluted components at around 284.8, 286.0, and 288.8 eV, corresponding to C-C/C═C, C-N, and C-O/C═O bonding configurations, respectively. As shown in Fig. 1g, the N 1 s XPS spectra of Fe-N_4 and Fe-N_2O_2 were deconvoluted into five components located at 398.7, 400.0, 400.5, 401.5, and 404.5 eV, corresponding to pyridinic N, Fe-N, pyrrolic N, graphitic N, and oxidized N, respectively [41]. Compared with metal-free N_2O_2, Fe-N_2O_2 exhibited markedly reduced proportions of pyridinic N and pyrrolic N, indicating that Fe loading altered the defect-related nitrogen environment and thereby confirming the coordination of Fe atoms. In addition, the Fe-N content in Fe-N_4 (21.5 at%) was substantially higher than that in Fe-N_2O_2 (9.99 at%) (Table S6), suggesting that O atoms partially replaced pyridinic N and thus modulated the local coordination environment of Fe [42]. The Fe 2p spectrum (Fig. S15b and Table S7) showed characteristic doublet peaks at 709.7 and 711.4 eV, assigned to Fe^{2+} and Fe^{3+}, respectively. Meanwhile, the O 1 s spectrum displayed four peaks at 531.0, 531.8, 533.0, and 534.2 eV, corresponding to Fe-O, C-O, C═O, and H_2O, respectively (Fig. 1h and Table S8). In Fe-N_2O_2, the Fe-O content reached 9.92 at%, while the proportions of C═O and C-O decreased after Fe loading, further supporting Fe-O coordination and the presence of N,O-coordinated Fe sites, as well as the feasibility of anchoring isolated Fe atoms using the Salophen ligand.

3.2. Catalytic performance

To evaluate the effect of N,O co-coordination-induced electronic structure modulation on PMS activation, PN was selected as a model pollutant to assess the catalytic performance of the prepared materials. As shown in Fig. 2a, pristine N_2O_2 and Fe-N_2O_2 exhibited appreciable adsorption capacities toward PN, achieving removal efficiencies of 35.7% and 22.4% within 5 min, respectively. By contrast, PMS alone and Fe-N_4 alone removed only 1.94% and 5.62% of PN over the same period, and the adsorption-based removal efficiency of Fe-N_2O_2 was 3.97 times that of Fe-N_4. These results indicate that adsorption contributes to pollutant enrichment, whereas the subsequent catalytic degradation mainly depends on PMS activation. The Fe^{2+}/PMS and N_2O_2/PMS systems showed limited activity. Their PN removal efficiencies were only 5.02% and 28.1%, respectively. These results indicate that PMS could not be efficiently activated by dissolved Fe ions or by the N,O-coordinated framework alone. After PMS addition, Fe-N_2O_2 achieved complete PN removal within 5 min. Kinetic analysis further confirmed the superior activity of Fe-N_2O_2. The pseudo-first-order rate constant (k_{obs}) reached 2.51 min^{-1}. This value was 70.8 and 1.58 times higher than those of the N_2O_2/PMS and Fe-N_4/PMS systems, respectively (Fig. S16). Because the two catalysts exhibited substantially different Fe loadings, Fe-normalized activity was used as a complementary comparison. The results showed that the Fe-content-normalized performance of the Fe-N_2O_2/PMS (1.25 min^{-1}) system was approximately five times higher than that of the Fe-N_4/PMS (0.25 min^{-1}) system. Similarly, Fe-normalized TOF_{app} analysis revealed a five-fold higher activity for Fe-N_2O_2/PMS (4.93 min^{-1}) than Fe-N_4/PMS (0.99 min^{-1}), supporting its higher Fe-normalized apparent

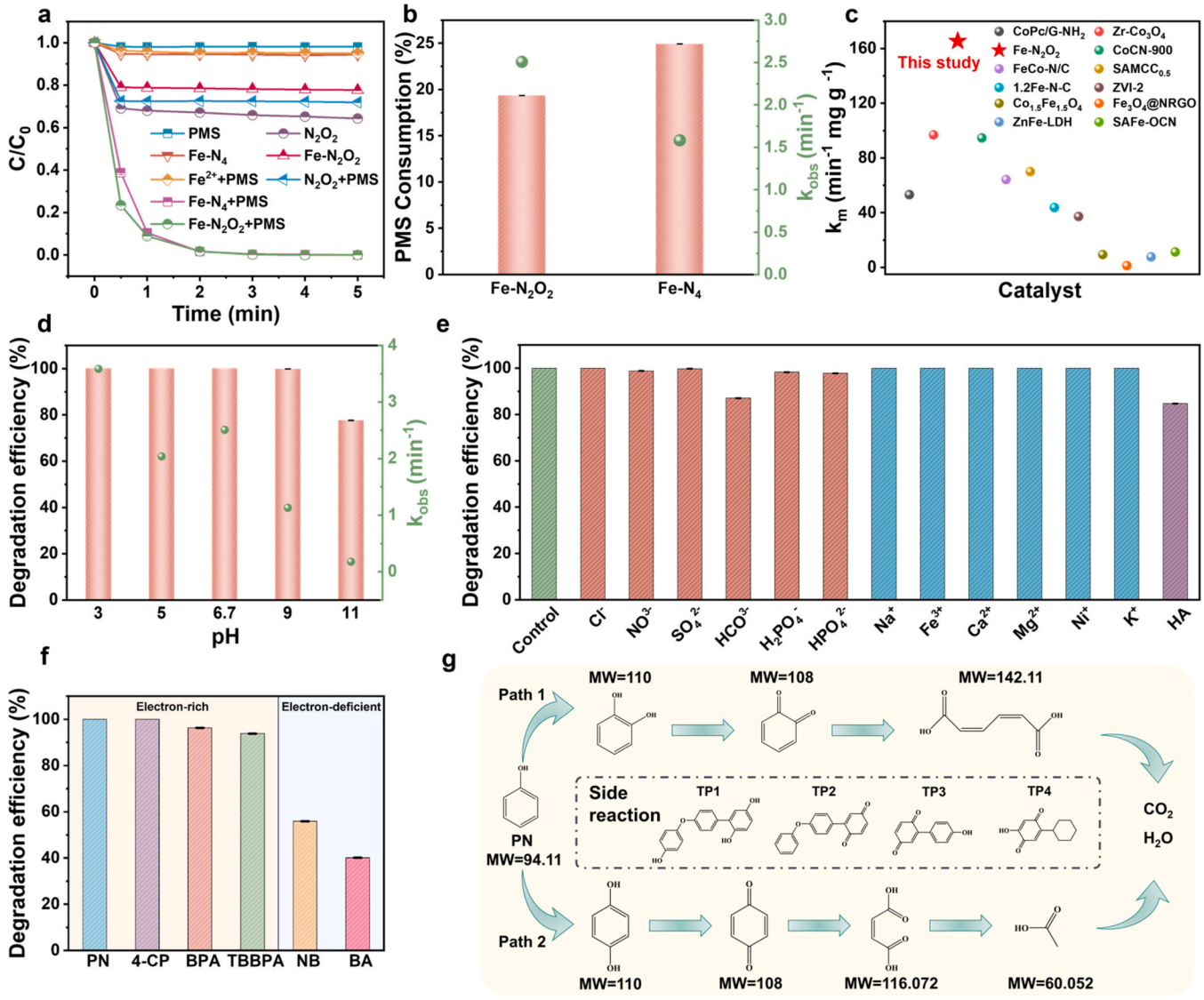


Fig. 2. Evaluation of catalytic performance. (a) Comparison of PN degradation behavior among different reaction systems; (b) the comparison of observed k_{obs} and PMS consumption; (c) specific activity comparison for organic pollutant degradation between the Fe-N_2O_2/PMS system and reported carbon-based SACs/PMS systems; (d) influence of pH on PN degradation in the Fe-N_2O_2/PMS system; (e) degradation performance of the Fe-N_2O_2/PMS system in the presence of coexistent ions and HA; (f) degradation efficiency of multiple phenolic compounds in Fe-N_2O_2/PMS system; (g) proposed transformation pathways of PN. Reaction conditions: $[PN]_0 = 10$ mg L^{-1}, $[PMS]_0 = 1.0$ mM, $[catalyst]_0 = 0.15$ g L^{-1}, initial pH = 6.7.

activity. However, differences in Fe loading, surface area, pore structure, defect density, adsorption, and accessible-site density may also affect the observed catalytic behavior. Accordingly, the enhanced catalytic performance is attributed to the combined effects of N,O-coordination-induced electronic regulation and these material properties. The Fe-normalized activity and TOFapp therefore serve only as complementary apparent-activity comparisons rather than intrinsic activity metrics. Moreover, PMS consumption analysis using RhB decolorization under Co-ion-activated PMS conditions [43] showed that Fe-N_2O_2 achieved efficient PN degradation with only 19.4% PMS consumption (Fig. 2b and Fig. S17). This result indicates limited oxidant consumption under the tested conditions, although a complete oxidant balance cannot be established from the current data. The specific activity (k_m) reached 165.5 min^{-1} mg g^{-1}, surpassing that of most reported PMS-based advanced oxidation process catalysts (Fig. 2c and Table S9). Taken together, the catalytic advantage of Fe-N_2O_2 should be interpreted as the combined outcome of its N,O-coordinated electronic environment and associated material properties.

The dosages of Fe-N_2O_2 and PMS in the Fe-N_2O_2/PMS system were systematically optimized, and the optimal conditions were identified as 0.15 g L^{-1} Fe-N_2O_2 and 1 mM PMS. Considering the trade-off between kinetic enhancement and reagent consumption, 0.15 g L^{-1} was selected as the optimal catalyst dosage (Fig. S18). When the PMS concentration increased to 1 mM, the k_{obs} value reached 2.51 min^{-1} (Figs. S19a and S19b). However, further increasing the PMS concentration did not substantially enhance PN degradation (Fig. S19c), likely because the number of available active sites for PMS activation was limited. Therefore, 1 mM PMS was used in subsequent experiments.

The applicability of the catalyst was further evaluated under different reaction conditions. As depicted in Fig. 2d and Fig. S20, the Fe-N_2O_2/PMS system achieved complete PN removal over a wide pH range of 3–9. Under alkaline conditions, however, PN degradation was moderately suppressed, mainly because hydrogen monopersulfate (HSO_5^-) was converted to SO_5^{2-} (pKa = 9.40), while PN (pKa ≈ 9.99) was deprotonated to PN^-, both of which were unfavorable for the catalytic process [44]. The effects of coexisting ions were also examined (Fig. 2e). Except for bicarbonate (HCO_3^-) and humic acid (HA), which reduced PN degradation to 86.0% and 84.7% within 5 min, respectively, all other

tested ions allowed complete PN removal within 5 min (Fig. S21). Among these species, the enhancement of PN degradation upon Cl^- addition may be related to secondary reactive chlorine species formed in the PMS-containing system [45]. The addition of HCO_3^- increased the solution pH and negatively affected PN degradation [46], while HPO_4^{2-} reacted with radicals and thereby inhibited the degradation reaction [47]. These findings demonstrate that the Fe-N_2O_2/PMS system retains robust degradation performance in the presence of common water constituents. They also suggest that non-radical pathways may contribute to PN degradation. This possibility was further investigated through ROS quenching and EPR analyses.

As illustrated in Fig. S22, the total organic carbon (TOC) removal performance of the Fe-N_2O_2/PMS system was systematically evaluated to assess its TOC removal performance. After 30 min of reaction, the TOC removal reached 73.1%. Notably, complete PN removal within 5 min reflects the disappearance of the parent pollutant, whereas TOC reduction indicates its further oxidative transformation. Because a complete carbon balance was not established, the TOC decrease alone cannot be interpreted as evidence of complete mineralization. The observed TOC removal and further oxidative transformation are likely associated with the N,O-coordinated Fe sites, which promote ROS generation and facilitate more complete oxidative decomposition [48]. The environmental adaptability of the system was further assessed under different pH conditions and in the presence of common coexisting species. Except at pH= 5 and in the presence of HPO_4^{2-}, the Fe-N_2O_2/PMS system maintained relatively high TOC removal under most tested conditions. These results indicate robust anti-interference capability and support the practical potential of the Fe-N_2O_2/PMS system for water treatment. At pH= 5, PN was nearly completely degraded, whereas TOC removal decreased to approximately 40%, suggesting that acidic conditions limited the further oxidation of intermediates and led to greater intermediate accumulation than at pH 6.7.

As illustrated in Fig. 2f, apart from PN, the Fe-N_2O_2/PMS system also exhibited excellent degradation performance (>95.0%) toward other electron-rich pollutants, such as 4-chlorophenol (4-CP), bisphenol A (BPA), and tetrabromobisphenol A (TBBPA), within 5 min. In contrast, the degradation of electron-deficient pollutants, such as benzoic acid (BA) and nitrobenzene (NB), was much less efficient, with k_{obs} values of only 0.07 min^{-1} and 0.06 min^{-1}, respectively (Fig. S23). The substrate-dependent oxidation behavior of Fe-N_2O_2 correlated with the ionization potentials of the tested pollutants, indicating that the selective degradation of electron-rich phenolic compounds was closely associated with non-radical oxidation pathways involving $^1O_2$ and electron-transfer processes [49]. The degradation rates of halophenolic compounds (Fig. S24) increased in the order F < Cl < Br, with bromophenol showing a higher rate constant (3.39 min^{-1}) than PN (2.51 min^{-1}). This trend qualitatively agrees with the substituent effect of halogens, as the increasing polarizability from F to Br may facilitate the oxidative attack of electron-rich phenolic substrates. These substrate-dependent reactivity patterns, together with the strong anti-interference performance of the Fe-N_2O_2/PMS system, further suggest the involvement of selective ROS pathways, which were subsequently investigated through quenching, EPR, and electrochemical analyses.

Liquid chromatography-mass spectrometry (LC-MS) analysis identified six intermediates during PN degradation in the Fe-N_2O_2/PMS system (Fig. S25 and Table S10). As shown in Fig. 2g, PN was first hydroxylated to catechol and hydroquinone (MW = 110) [50,51], followed by further oxidation to benzoquinone (MW = 108). Subsequent ring opening generated small carboxylic acids, such as fumaric acid (MW = 116), supporting progressive oxidative transformation of PN and remaining consistent with the observed 73.1% TOC reduction after 30 min. Although phenolic intermediates and benzoquinone are difficult to detect due to their low ionization potentials and high reactivity [52], the detected phenol-quinone adducts support the proposed pathway. The structures of TP1–TP4 were tentatively assigned based on the corresponding MS signals in Fig. S25 and are presented as proposed rather than definitive intermediates.

3.3. ROS identification and catalytic mechanism

Heteroatom modulation has been widely recognized as an effective strategy for tuning the coordination environment of single-atom catalytic sites and steering ROS generation pathways [21]. To elucidate the dominant ROS and catalytic mechanisms in the Fe-N_2O_2/PMS and Fe-N_4/PMS systems, quenching experiments, electron paramagnetic resonance (EPR), and electrochemical analyses were systematically conducted [53,54]. Tert-butanol (TBA) was used as a scavenger for hydroxyl radicals (·OH), whereas methanol (MeOH) was employed to quench both sulfate radicals ($SO_4^{\cdot-}$) and hydroxyl radicals (·OH). Furthermore, p-benzoquinone (p-BQ) and furfuryl alcohol (FFA) were used as quenching agents for superoxide radicals ($O_2^{\cdot-}$) and singlet oxygen ($^1O_2$), respectively [24,25,55,56]. Dimethyl sulfoxide (DMSO) was further introduced to examine the possible involvement of high-valent metal-oxo intermediates, specifically Fe(IV)=O, in PMS activation and pollutant degradation [57].

To probe the possible participation of Fe(IV)=O, quenching tests were first performed at different scavenger concentrations (Fig. S26a). As shown in Fig. 3a, both catalysts still achieved complete PN degradation in the presence of DMSO, although the reaction rate of Fe-N_2O_2/PMS decreased to 0.91 min^{-1}. This substantial decrease suggests the possible involvement of DMSO-sensitive oxidative species, including high-valent Fe–oxo intermediates [58]. Since abundant Fe(IV)=O formation usually requires favorable redox conditions or additional driving forces, its dominant contribution is considered less likely in the present system [53,59]. However, because DMSO is not a selective probe and direct spectroscopic evidence is unavailable, the formation and quantitative contribution of Fe(IV)=O cannot be conclusively confirmed or excluded. Scavengers may also consume PMS or compete with pollutants for catalyst surface sites. These effects could lead to an underestimation of the $^1O_2$ contribution [60]. Therefore, the appropriate concentration of the $^1O_2$ inhibitor was determined in advance (Fig. S26). In the Fe-N_4/PMS system, p-BQ markedly inhibited PN degradation (Fig. 3a and Fig. S27b). In contrast, quenching $SO_4^{\cdot-}$, ·OH, or $^1O_2$ had little effect on the degradation kinetics. These results indicate that $O_2^{\cdot-}$ was the dominant reactive species in this system. By contrast, p-BQ and FFA suppressed PN degradation in the Fe-N_2O_2/PMS system by 72.76% and 54.73%, respectively (Fig. 3a and Fig. S27a). This result indicates the involvement of both $O_2^{\cdot-}$ and $^1O_2$. Notably, the pronounced inhibition caused by p-BQ suggests that $O_2^{\cdot-}$ or $O_2^{\cdot-}$-related pathways play a crucial role in PN degradation. These findings suggest that Fe-N_2O_2 sites facilitate the conversion of $O_2^{\cdot-}$ into $^1O_2$, while $O_2^{\cdot-}$ itself may still contribute to the initial oxidation of PN. Because of its anionic character, $O_2^{\cdot-}$ generally exhibits limited reactivity toward electron-rich aromatic centers [13]. In contrast, $^1O_2$ can selectively attack such sites, making the Fe-N_2O_2/PMS system more favorable for selective pollutant oxidation [61]. This conclusion was further corroborated by quenching experiments using L-histidine as an additional $^1O_2$ scavenger (Fig. S26b) [60].

EPR characterization was performed using 5,5-dimethyl-1-pyrroline-N-oxide (DMPO) and 2,2,6,6-tetramethyl-4-piperidinol (TEMP) as spin-trapping agents [62]. DMPO-EPR signals assigned to ·OH, $SO_4^{\cdot-}$, and $O_2^{\cdot-}$ were detected in both systems (Fig. 3b). Under the same measurement conditions, the corresponding DMPO signals of Fe-N_2O_2 were weaker than those of Fe-N_4. As shown in Fig. 3c, a distinct TEMP-$^1O_2$ triplet signal appeared in the Fe-N_2O_2/PMS system, whereas no such signal was observed in the Fe-N_4/PMS system. This result provides direct EPR evidence for $^1O_2$ generation in the Fe-N_2O_2/PMS system and indicates that $^1O_2$ participates as an important reactive species. Moreover, the degradation rate decreased in heavy water (D_2O) rather than showing the classical solvent-isotope enhancement expected for a purely $^1O_2$-controlled process (Fig. S28). This observation suggests that $^1O_2$ participates in PN oxidation but is not an exclusive pathway, with

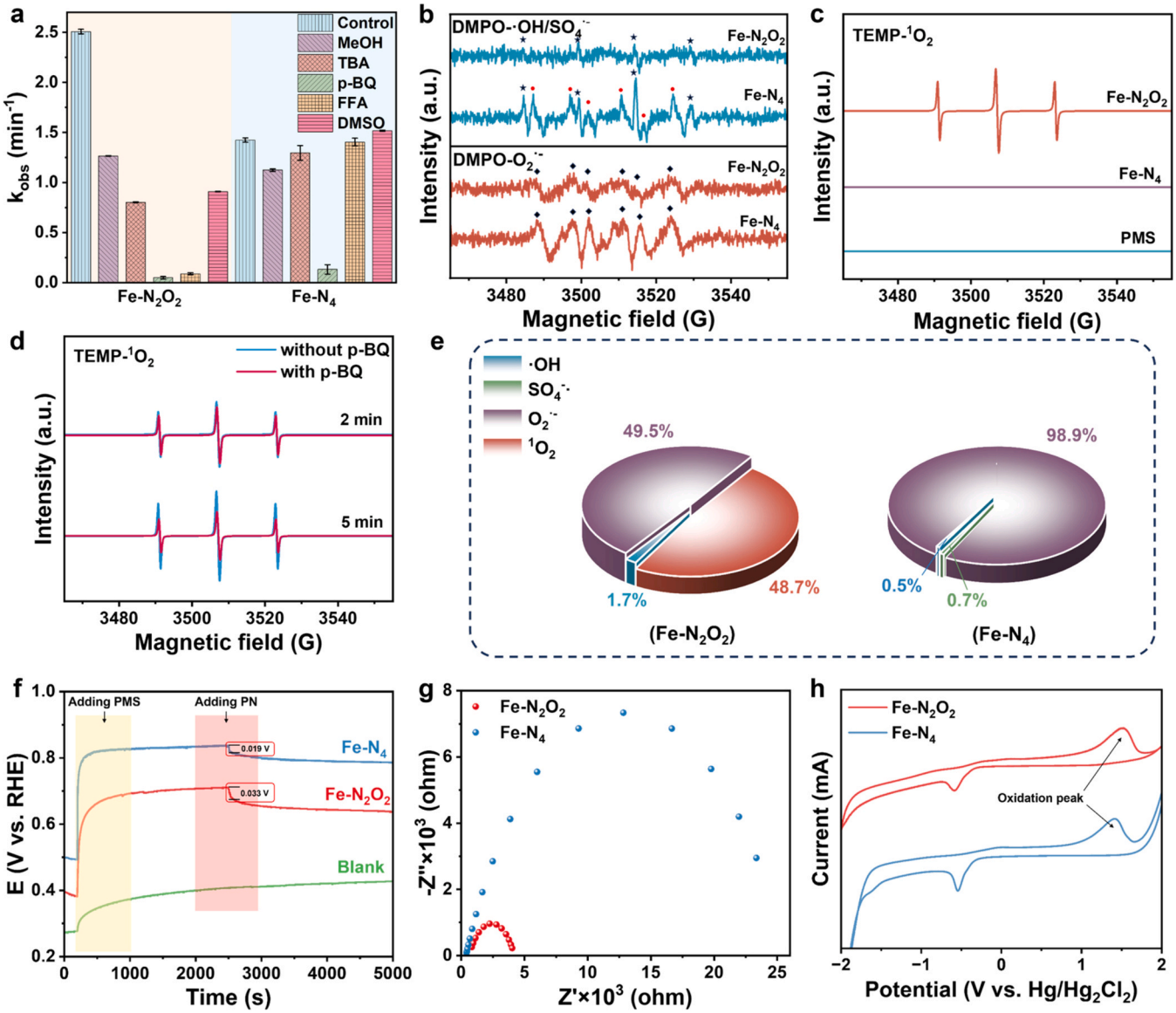


Fig. 3. (a) Degradation of PN in the Fe-N_2O_2/PMS system with the presence of various quenching agents; ROS identification and catalytic mechanism EPR spectrum of the different systems captured by DMPO and TEMP for detection of (b)·OH, $O_2^{·-}$, $SO_4^{·-}$, and (c-d) $^1O_2$; (e) apparent relative ROS involvement estimated from quenching experiments (semi-quantitative); (f) open-circuit potential profiles of Fe-N_2O_2 and Fe-N_4 recorded during the sequential addition of PMS solution (1 mM) and PN; (g) EIS plots of Fe-N_2O_2 and Fe-N_4; (h) CV curves of Fe-N_2O_2 and Fe-N_4. Reaction conditions: $[PN]_0$ = 10 mg L^{-1}, $[PMS]_0$ = 1.0 mM, $[catalyst]_0$ = 0.15 g L^{-1}, initial pH = 6.7.

electron transfer and other PMS activation routes also contributing [63]. After $O_2^{·-}$ quenching, the $^1O_2$ signal was suppressed (Fig. 3d), suggesting that $O_2^{·-}$-mediated conversion may contribute to $^1O_2$ generation [64]. However, the present results cannot distinguish this pathway from PMS self-decomposition or direct $^1O_2$ formation through catalyst–PMS complexes. Therefore, these routes are considered possible coexisting pathways rather than independently established mechanisms. Semi-quantitative quenching analysis suggested comparable apparent involvement of $^1O_2$ and $O_2^{·-}$ in the Fe-N_2O_2/PMS system. In the Fe-N_4/PMS system, the quenching-derived apparent involvement index of $O_2^{·-}$ reached 98.9% (Fig. 3e). Because the quenchers are not fully selective and the ROS pathways are interconnected, the percentages in Fig. 3e should be regarded only as semi-quantitative indicators for comparing relative ROS involvement under the tested conditions, rather than as absolute, independent, or additive pathway contributions. Combined with the quenching results, these findings support the view that N,O co-coordination promoted further $^1O_2$ generation in the Fe-N_2O_2/PMS system. The generated $^1O_2$ likely attacked electron-rich aromatic regions through a cycloaddition-type process, thereby contributing to substantial oxidative transformation and supporting a synergistic degradation pathway involving both radical and non-radical processes [65]. Nevertheless, contributions from interfacial electron transfer and other PMS activation pathways cannot be excluded, while a possible involvement of high-valent Fe–oxo species also remains to be further verified.

Since previous reports have indicated that co-adsorption of PMS and pollutants on catalyst surfaces may trigger direct electron-transfer pathways during pollutant oxidation [66], open-circuit potential tests (OCPT) were conducted to probe the electron-transfer process (Fig. 3f). After PMS addition at 200 s, the potentials of both Fe-N_2O_2/PMS and Fe-N_4/PMS increased markedly, indicating catalyst–PMS complex formation accompanied by electron redistribution. Subsequent PN addition caused a larger potential drop in Fe-N_2O_2/PMS (0.033 V) than in Fe-N_4/PMS (0.019 V), whereas no obvious change occurred in the blank group, supporting more pronounced interfacial electron transfer in the Fe-N_2O_2 system.

This conclusion was further supported by electrochemical impedance spectroscopy (EIS). As depicted in Fig. 3g, the charge-transfer resistance of Fe-N_2O_2 was approximately five times lower than that of Fe-N_4, indicating that the four-coordinate Fe-N_4 structure hindered electron migration because of stronger electron localization [25,67,68], whereas oxygen incorporation improved the electronic conductivity of the catalyst. Linear sweep voltammetry (LSV) further revealed distinct redox behavior between the two catalysts. Fe-N_2O_2 exhibited oxidation peaks at 1.05 and 1.50 V (Fig. S29a), whereas Fe-N_4 showed only one peak near 1.50 V (Fig. S29b). Considering the coexistence of Fe^{2+} and Fe^{3+} identified by XPS, the additional 1.05 V peak may be associated with a Fe-centered redox process involving Fe^{2+}/Fe^{3+}. These results indicate that N,O coordination alters the redox behavior of the Fe sites and facilitates interfacial electron transfer [69]. As shown in Fig. 3h, cyclic voltammetry (CV) measurements further showed a higher oxidation peak potential for Fe-N_2O_2. The current response increased after the addition of both catalysts, which was attributed to the formation of catalyst-PMS complexes [69,70]. Notably, after PN was introduced into the Fe-N_2O_2/PMS system, the intensity of the oxidation peak decreased, indicating that electron transfer occurred between PN and PMS on the catalyst surface [71]. In contrast, the Fe-N_4/PMS/PN system showed only a slight leftward shift of the oxidation peak with minimal current variation, reflecting less efficient electron transfer. Collectively, OCP reflects the potential response associated with catalyst–PMS interaction and PN-induced electron transfer, EIS demonstrates facilitated charge migration, and LSV/CV reveal enhanced redox and interfacial charge-transfer behavior. These complementary results indicate that N,O coordination promotes electron migration and interfacial electron transfer in Fe-N_2O_2 during PMS activation [24]. Although quenching, EPR, and electrochemical results support the proposed mechanism, the contribution of each pathway requires further operando investigation.

3.4. *Theoretical calculations of N,O-coordination effect in single-Fe-atom catalysts*

To further understand the experimentally observed charge-transfer behavior and ROS pathway shift, density functional theory (DFT) calculations were performed to investigate how N,O co-coordination regulates the electronic structure of Fe sites and PMS activation. The calculations employed idealized models and focused on PMS adsorption, interfacial charge redistribution, and O* formation rather than the complete ROS generation network or reaction kinetics [24]. The EXAFS-fitted Fe-N and Fe-O coordination numbers were 2.6 ± 0.2 and 2.5 ± 0.5, with bond lengths of 2.04 ± 0.03 and 1.87 ± 0.03 Å, respectively, whereas the idealized DFT model contained two N and two O ligands with optimized Fe-N and Fe-O bond lengths of 1.86 and 1.93 Å. These differences arise because EXAFS reflects the ensemble-averaged local environment of real Fe sites, whereas DFT represents an isolated, optimized N,O-coordinated model. Thus, the DFT structure is used for comparative electronic-structure and PMS-activation analysis rather than as an exact reproduction of the EXAFS-derived local structure.

The oxygen atoms that could potentially coordinate with the Fe center were denoted as O1, O2, and O3. As illustrated in Fig. 4a, both Fe-N_2O_2 and Fe-N_4 exhibited similar adsorption trends toward PMS. In both systems, the O2 site showed relatively weak adsorption. The O1 site was the most favorable adsorption site for both catalysts, with similar adsorption energies (-1.25 and −1.29 eV), indicating effective PMS anchoring in both systems. O1 was identified as the preferred adsorption configuration and determined the initial anchoring mode of PMS. O3 was further considered because of its closer association with peroxide-bond activation. Therefore, under the O1 and O3 adsorption configurations, the frontier molecular orbital distribution, electron-transfer capability, and activation Gibbs free energy change (ΔG) of the catalysts were further analyzed.

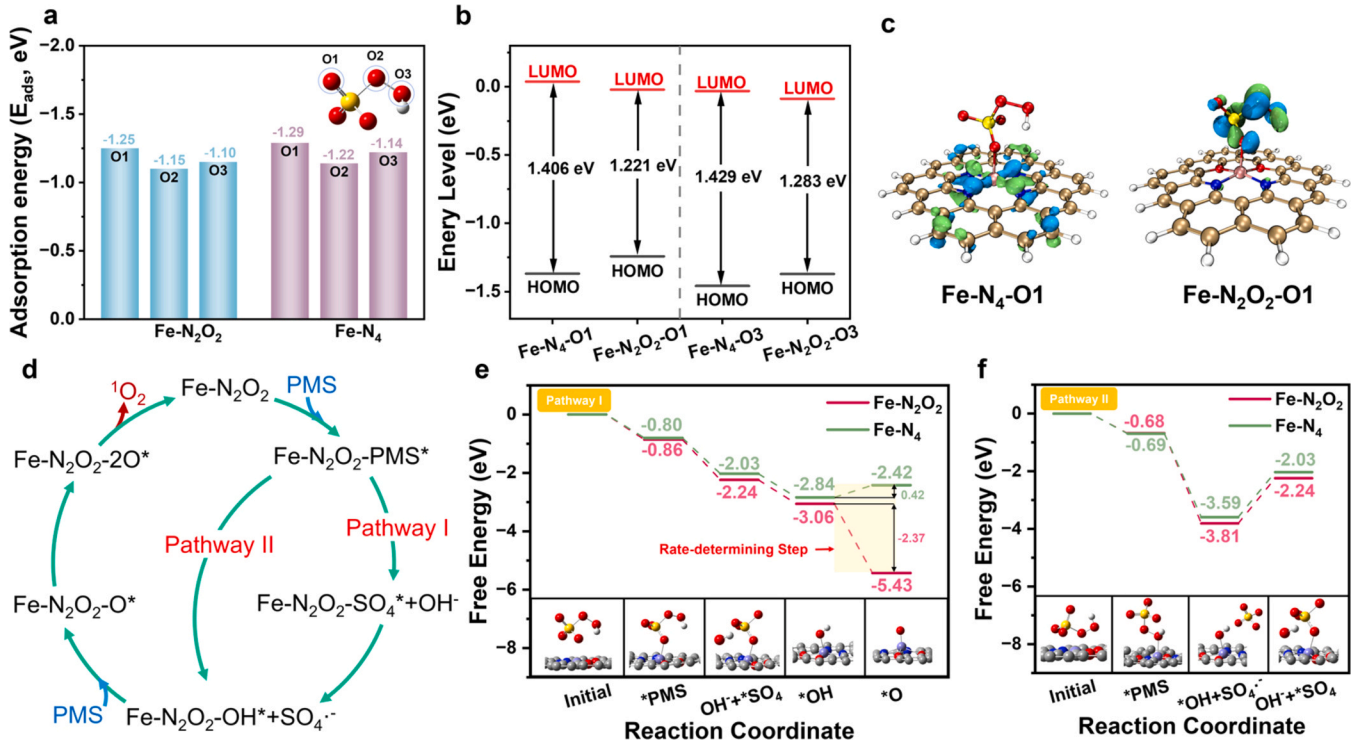


Fig. 4. (a) Adsorption energies (E_{ads}) of two catalysts on different PMS oxygen sites; (b) HOMO/LUMO energy level diagrams of the two catalyst systems after PMS adsorption at the O1 and O3 sites; (c) Natural Bond Orbital (NBO) diagram of a 3d lone pair electron on the Fe atom for PMS adsorption at the O1 site on Fe-N_4 and Fe-N_2O_2; (d) Possible mechanism step diagram of $^1O_2$ generation by PMS activation; Energy profiles of PMS activation at the (e) O1 and (f) O3 sites for the Fe-N_4/PMS and Fe-N_2O_2/PMS systems.

As shown in Fig. 4b, molecular reactivity can be effectively reflected by the highest occupied molecular orbital (HOMO) and lowest unoccupied molecular orbital (LUMO) energy levels, which are commonly used as global reactivity descriptors. Compared with Fe-N_4, Fe-N_2O_2 exhibited a higher HOMO energy level and a narrower HOMO-LUMO gap under both the O1 and O3 adsorption configurations. Notably, at the O1 site, the energy gap decreased from 1.41 eV for Fe-N_4 to 1.22 eV for Fe-N_2O_2. This narrower gap indicates a greater tendency for electronic redistribution. Together with the orbital distribution, this result suggests enhanced interfacial charge-transfer capability between Fe-N_2O_2 and PMS.

Subsequently, natural bond orbital (NBO) analysis was conducted to evaluate electron transfer between the Fe centers and PMS in the two catalysts. In the isolated state, Fe-N_2O_2 showed a higher Fe charge (+2.01 e) than Fe-N_4 (+1.90 e), consistent with the higher Fe oxidation state observed by XANES and the reduced electron density at the Fe center (Fig. S30). When PMS was adsorbed through the O1 site, the Fe charge in Fe-N_4 decreased from + 1.90 e to −0.46 e. This 2.36 e change suggests pronounced electron accumulation at the Fe center. In Fe-N_2O_2, the Fe charge decreased from + 2.01 to + 0.66 e, accompanied by charge redistribution over the coordinating N and O atoms. As shown in Fig. 4c, the Fe 3d electron cloud in Fe-N_2O_2 extended more markedly toward PMS, displaying stronger orbital directionality and spatial overlap than Fe-N_4. A similar trend was observed for O3-site adsorption. NBO analysis revealed that N,O co-coordination disrupted the symmetric Fe-N_4 environment and induced Fe 3d orbital polarization, thereby optimizing the electronic structure of the Fe active center and consequently altering the PMS activation pathway (Fig. S31).

This charge-transfer mode reduced electron accumulation at the Fe center [72] and promoted more directional charge migration between Fe-N_2O_2 and PMS (Fig. 3g). To further elucidate the energetic differences in PMS activation between Fe-N_2O_2 and Fe-N_4, the thermodynamics of selected activation steps at the O1 and O3 sites were compared (Fig. 4e). At the O1 site, the PMS activation sequence can be described as PMS → PMS* → SO_4* + OH^- → OH* → O*, where * denotes an adsorbed intermediate. After PMS adsorption on the active site, O-O bond cleavage occurs first to generate adsorbed SO_4* and free OH^-. This step was thermodynamically favorable on both catalysts, with ΔG values of −1.38 eV for Fe-N_2O_2 and −1.23 eV for Fe-N_4. A subsequent substitution process then yields adsorbed OH*, suggesting that both catalysts exhibit stronger affinity for hydroxyl species than for the SO_4* fragment. At the O3 site, PMS also undergoes initial O-O bond cleavage, but direct substitution of SO_4* by OH* is thermodynamically unfavorable, implying that catalyst-bound OH* species are more likely formed at distinct adsorption sites and act as essential precursors for subsequent elementary steps.

Among the modeled steps, the largest energetic difference between the two catalysts was observed for the OH* → O* conversion. For Fe-N_2O_2, the ΔG for the OH* → O* step is −2.37 eV, indicating a spontaneous process. In contrast, the same step on Fe-N_4 involves a positive ΔG of 0.42 eV and is therefore thermodynamically less favorable. This energetic difference indicates that O* formation is thermodynamically more favorable on Fe-N_2O_2. Previous studies have proposed O*-related pathways for $^1O_2$ formation [73]. Overall, these results indicate that N,O co-coordination modifies the local electronic environment of Fe single-atom sites and lowers the ΔG of O* formation, consistent with the experimentally observed involvement of $^1O_2$ during PMS activation. However, the DFT calculations should be viewed as a comparative theoretical analysis rather than a complete description of the $^1O_2$ formation mechanism, given the simplifications inherent in the idealized model.

3.5. Potential practicability and continuous operation tests

To evaluate the operational feasibility of the Fe-N_2O_2/PMS system under laboratory conditions, its durability and reusability were further examined through cycling experiments, continuous-flow tests, and post-reaction structural characterization. Fe-N_2O_2 retained measurable catalytic activity over the first four consecutive cycles (Fig. 5a). Its crystal structure, FTIR spectra, and Raman spectra remained largely unchanged (Fig. S32). Therefore, the activity decay was more likely associated with surface-state evolution rather than bulk structural collapse. Moreover, only 0.0017 mg L^{-1} of Fe ions (0.006%) was detected in the post-reaction solution, indicating the absence of secondary pollution.

To clarify the origin of activity loss, XPS was performed before and after catalysis. The results showed that the proportion of C-N bonds in Fe-N_2O_2 decreased by 4.30 at% after reaction (Fig. S33a and Table S5). In addition, the Fe-N content increased by 4.45 at%, whereas the Fe-O content decreased by 6.36 at% (Fig. S33b-d, Table S6, and Table S8), indicating that the coordination environment of Fe sites was altered during catalysis. Such deactivation was likely associated with the occupation of active sites by PN-derived intermediates. Notably, the used catalyst was regenerated by thermal treatment at 600 °C for 2 h under N_2, followed by cooling, washing, and drying [74]. After regeneration, the Fe content remained stable at 1.95 wt%, and PN degradation efficiency recovered to above 95% (Fig. 5a), confirming the effective recovery of catalytic activity.

The applicability of the Fe-N_2O_2/PMS system was further verified in different water matrices, including tap water, river water, lake water, and pond water. As shown in Fig. 5b, these complex matrices exerted no significant adverse effect on PN removal, which may be related to the relatively strong resistance of $^1O_2$ to interference from common background constituents in real waters [73,75]. The aqueous TOC removal was further evaluated in different water matrices. TOC removal reached 83.22% in tap water and remained around 75% in river and lake water. Because these matrices contain background organic constituents and a complete carbon balance was not established, these values are reported as aqueous TOC removal rather than PN mineralization efficiencies. Together with the maintained PN removal, these results indicate that the Fe-N_2O_2/PMS system retains appreciable oxidation performance under the tested water-matrix conditions.

To facilitate catalyst recovery, polyacrylonitrile (PAN) was used primarily as a physical membrane support, and PAN, Fe-N_4/PAN, and Fe-N_2O_2/PAN membranes were fabricated by electrospinning. SEM images (Fig. S34) showed that the pristine PAN membrane exhibited a smooth fibrous network, whereas the Fe-N_4- and Fe-N_2O_2-loaded membranes displayed obvious particle deposition on the fiber surfaces (Fig. S35 and Fig. 5c), confirming successful catalyst loading. The as-prepared membranes were then assembled into a custom-made transparent flow cell (Fig. 5d) for continuous degradation experiments. Under continuous-flow conditions, the Fe-N_2O_2/PAN membrane maintained > 94.9% PN removal within 36 h (Fig. 5e), whereas the Fe-N_4/PAN membrane achieved approximately 50% removal. This difference can be attributed to its weaker adsorption capacity and lower intrinsic catalytic activity. The continuous-flow test used a lower PN concentration (1 vs. 10 mg L^{-1} in batch tests) and was therefore intended to assess sustained operation rather than direct batch comparison. Under extended operation for 72 h, the Fe-N_2O_2/PAN membrane showed a gradual decrease in PN removal efficiency, likely due to the accumulation of oxidation intermediates and by-products that partially block Fe-N_2O_2 active sites and hinder PMS activation [76]. The blank PAN membrane was also evaluated, confirming that PN removal was dominated by the supported catalyst rather than PAN itself. Thus, PAN mainly provided mechanical support and facilitated catalyst immobilization and recovery. Overall, the membrane experiment demonstrates the feasibility of sustained continuous-flow operation under the specified laboratory conditions. However, the relatively high PMS-to-PN ratio, the energy demand associated with thermal regeneration at 600 °C, and the absence of a complete set of engineering parameters limit direct extrapolation to practical water treatment. Further optimization of oxidant dosage, hydraulic conditions, regeneration strategy, and long-term operation in real wastewater is therefore required.

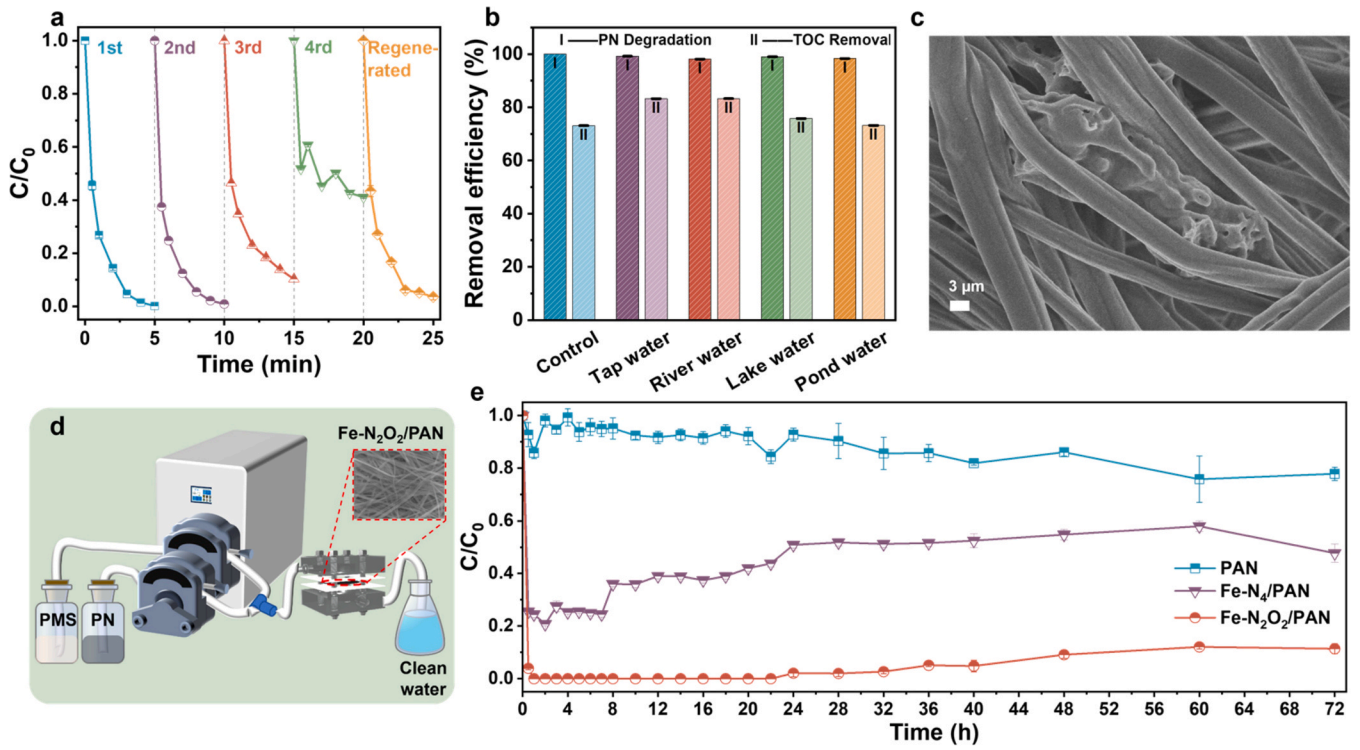


Fig. 5. (a) Stability test of the Fe-N_2O_2/PMS system; (b) removal performance of the Fe-N_2O_2/PMS system in different water matrices; (c) SEM images of the Fe-N_2O_2/PAN membrane; (d) schematic diagram of a continuous flow catalytic device; (e) continuous operation test of PN removal efficiency in the continuous flow system. Experimental conditions: $[PN]_0$ = 1 ppm, $[PMS]_0$ = 1 mM, pH = 7.0, and T = 25 °C, average flow rate 2 mL min^{-1}.

4. Conclusion

In summary, Schiff-base pre-coordination was employed to construct an N,O-coordinated Fe single-atom catalyst. Structural and spectroscopic analyses supported the formation of N,O-coordinated Fe sites and the associated modulation of the Fe electronic structure. Fe-N_2O_2 exhibited a specific activity of 165.45 min^{-1} mg g^{-1} and 73.1% TOC removal within 30 min. The observed catalytic enhancement is considered to arise from the combined effects of coordination-induced electronic regulation and material properties. Combined experimental and theoretical results show that regulation of the Fe coordination microenvironment alters electron-density distribution, facilitates interfacial charge transfer, and lowers the ΔG of O* formation. These effects are consistent with the enhanced involvement of $^1O_2$ during PMS activation. Cycling and continuous-flow experiments further demonstrate operational feasibility under the specified laboratory conditions, while further optimization is required before practical water-treatment applicability can be established. These findings establish a structure–electronic property–reactivity relationship between Schiff-base-directed N,O coordination, Fe electronic redistribution, and PMS activation, providing a basis for coordination engineering of single-atom catalysts.

Declaration of Competing Interest

The authors declare the following financial interests/personal relationships which may be considered as potential competing interests: Liangzhong Li, Chengyu Hu, Juhai Liu, Chenyu Yang, Xiang He, Rui Shan, Haoran Yuan has patent A Method for Preparing a Nitrogen-Oxygen Co-coordinated Iron Single-atom Catalyst and Its Application in the Degradation of Phenolic Pollutants pending to Liangzhong Li. If there are other authors, they declare that they have no known competing financial interests or personal relationships that could have appeared to influence the work reported in this paper.

Acknowledgements

This work was supported by the National Natural Science Foundation of China (No. 42377489, 42407373) and the Inner Mongolia Autonomous Region Science and Technology Program Project (No. 2025YFHH0202). The numerical calculations in this paper have been done at Hefei advanced computing center. We thank the Shanghai Synchrotron Radiation Facility (SSRF), Shanghai, P. R. China for the EXAFS experiments.

Appendix A. Supporting information

Supplementary data associated with this article can be found in the online version at doi:10.1016/j.apcatb.2026.127622.

Data availability

Data will be made available on request.

References

[1] R. Guo, M. Cao, M. Hu, W. Deng, W. Zhang, Y. Gao, S. Ye, W. Zhou, J. Shi, Synthesis and toxicity of halogenated bisphenol monosubstituted-ethers: establishing a library for potential environmental transformation products of emerging contaminant, Chem. & Biodivers. 17 (2020) e2000481, https://doi.org/10.1002/cbdv.202000481.

[2] Y. Zhou, M. Nemati, Co-biodegradation of Phenol, o-Cresol, and p-Cresol in binary and ternary mixtures: evaluation of bioreactor performance and toxicity of treated effluents, Water Air & Soil. Pollut. 233 (2022) 133, https://doi.org/10.1007/s11270-022-05605-w.

[3] M. Du, H. Shi, R. Guo, W. Wu, J. Liu, P. Guo, J. Niu, Y. Ning, Q. Zheng, Mechanism and adsorption enhancement of metal-organic frameworks for the removal of phenolic pollutants: a review, J. Environ. Chem. Eng. 14 (2026) 123466, https://doi.org/10.1016/j.jece.2026.123466.

[4] M.J. Ahmed, I. Anastopoulos, F. Marrakchi, I.D. Manariotis, Recent progress on carbonaceous materials and their composites as adsorbents for phenolic pollutants: a review, J. Anal. Appl. Pyrolysis 195 (2026) 107629, https://doi.org/10.1016/j.jaap.2026.107629.

[5] Y. Duan, J. Liu, Q. Liu, T. Li, H. Zhao, Z. Shen, Remediation of characteristic contaminants in groundwater of chemical industrial by the activation of PMS: recent developments and challenges-a mini-review, Chin. Chem. Lett. (2025) 111120, https://doi.org/10.1016/j.cclet.2025.111120.
[6] K. Xu, Z. Feng, C. Li, Y. Li, M. Zhang, C. Gu, Z. Luo, L. Wang, Precision engineering of single-atom catalysts to enhance the peroxymonosulfate activation in Fenton-like reactions, Adv. Sustain. Syst. 10 (2026) e70488, https://doi.org/10.1002/adsu.70488.
[7] X. Zhang, T. Shi, Z. Li, G. Li, X. Han, S. Chen, C. Si, M. Wei, Nanoporous zero-valent transition metals for enhanced peroxymonosulfate activation toward phenolic pollutants degradation: performance, pathways, and DFT mechanism study, Small 22 (2026) e14503, https://doi.org/10.1002/smll.202514503.
[8] W. Miao, Y. Liu, D. Wang, N. Du, Z. Ye, Y. Hou, S. Mao, K. Ostrikov, The role of Fe-Nx single-atom catalytic sites in peroxymonosulfate activation: formation of surface-activated complex and non-radical pathways, Chem. Eng. J. 423 (2021) 130250, https://doi.org/10.1016/j.cej.2021.130250.
[9] L. Tang, S. Zhou, F. Li, L. Sun, H. Lu, Ozone micronano-bubble-enhanced selective degradation of oxytetracycline from production wastewater: the overlooked singlet oxygen oxidation, Environ. Sci. & Technol. 57 (2023) 18550–18562, https://doi.org/10.1021/acs.est.2c06008.
[10] Q. Zhou, C. Song, P. Wang, Z. Zhao, Y. Li, S. Zhan, Generating dual-active species by triple-atom sites through peroxymonosulfate activation for treating micropollutants in complex water, Proc. Natl. Acad. Sci. 120 (2023) e2300085120, https://doi.org/10.1073/pnas.2300085120.
[11] L. Wang, K. Xiao, H. Zhao, The debatable role of singlet oxygen in persulfate-based advanced oxidation processes, Water Res. 235 (2023) 119925, https://doi.org/10.1016/j.watres.2023.119925.
[12] S. Zhang, H. Zheng, P.G. Tratnyek, Advanced redox processes for sustainable water treatment, Nat. Water 1 (2023) 666–681, https://doi.org/10.1038/s44221-023-00098-1.
[13] R. Luo, M. Li, C. Wang, M. Zhang, M.A. Nasir Khan, X. Sun, J. Shen, W. Han, L. Wang, J. Li, Singlet oxygen-dominated non-radical oxidation process for efficient degradation of bisphenol A under high salinity condition, Water Res. 148 (2019) 416–424, https://doi.org/10.1016/j.watres.2018.10.087.
[14] C. Li, X. Xu, M. Liu, S. He, Y. Qian, Z. Li, Treatment of high-salinity organic wastewater by advanced oxidation processes: Research progress and prospect, J. Water Process. Eng. 60 (2024) 105272, https://doi.org/10.1016/j.jwpe.2024.105272.
[15] P.V. Nidheesh, G. Boczkaj, S.O. Ganiyu, A.A. Oladipo, K. Fedorov, R. Xiao, D. D. Dionysiou, Generation, properties, and applications of singlet oxygen for wastewater treatment: a review, Environ. Chem. Lett. 23 (2024) 195–240, https://doi.org/10.1007/s10311-024-01798-0.
[16] H.R. Ahmed, Heterogeneous catalysts in advanced oxidation processes: A comprehensive review on antibiotic removal from wastewater, Sep. Purif. Technol. 374 (2025) 133670, https://doi.org/10.1016/j.seppur.2025.133670.
[17] C. Yang, Q. Yao, L. Li, X. Xiao, L. Lu, C. Liu, C. Zhu, S. Zhan, H. Yuan, The isolated Ca-N_x sites in biochar boosting Fe catalyzed Fenton-like oxidation of Tris(2-chloroethyl) phosphate: Properties, mechanisms, and applications, Appl. Catal. B Environ. Energy 366 (2025), https://doi.org/10.1016/j.apcatb.2025.125056.
[18] Y. Zeng, J. Deng, N. Zhou, W. Xia, Z. Wang, B. Song, Z. Wang, Y. Yang, X. Xu, G. Zeng, C. Zhou, Mediated Peroxymonosulfate Activation at the Single Atom Fe-N_3O_1 Sites: Synergistic Degradation of Antibiotics by Two Non-Radical Pathways, Small 20 (2024) 2311552, https://doi.org/10.1002/smll.202311552.
[19] M.K. Panjwani, S.M. Ahmadzai, J. Li, Z. Luo, G. Eshaq, K. Xiao, H. Zeng, Heteroatom doping strategies in single-atom catalysts: tuning electronic structure for selective peroxymonosulfate activation, J. Mater. Chem. A 14 (2026) 12509–12539, https://doi.org/10.1039/D6TA00071A.
[20] N. Sun, C. Yue, Y. Tian, Z. Zhou, F. Liu, D-band center regulation of FeOCl via fluorine heteroatom doping for enhanced photo-Fenton degradation of chlorophenols, J. Environ. Chem. Eng. 14 (2026) 122994, https://doi.org/10.1016/j.jece.2026.122994.
[21] P. Yang, Z. Cao, Y. Long, D. Liu, W. Huang, S. Zhan, M. Li, Regulating the Local Electronic Structure of Copper Single Atoms with Unsaturated B,O-Coordination for Selective $^1O_2$ Generation, ACS Catal. 13 (2023) 12414–12424, https://doi.org/10.1021/acscatal.3c03303.
[22] S. Wei, M. Sun, J. Huang, Z. Chen, X. Wang, L. Gao, J. Zhang, Axial chlorination engineering of single-atom nanozyme: Fe-N_4Cl catalytic sites for efficient peroxidase-mimicking, J. Am. Chem. Soc. 146 (2024) 33239–33248, https://doi.org/10.1021/jacs.4c13335.
[23] Y. Dai, B. Liu, Z. Zhang, P. Guo, C. Liu, Y. Zhang, L. Zhao, Z. Wang, Tailoring the d-orbital splitting manner of single atomic sites for enhanced oxygen reduction, Adv. Mater. 35 (2023) 2210757, https://doi.org/10.1002/adma.202210757.
[24] Y. Long, Z. Cao, W. Wu, W. Liu, P. Yang, X. Zhan, R. Chen, D. Liu, W. Huang, Rational modulation of Fe single-atom electronic structure in a Fe-N2B4 configuration for preferential 1O2 generation in Fenton-like reactions, Appl. Catal. B Environ. Energy 344 (2024) 123643, https://doi.org/10.1016/j.apcatb.2023.123643.
[25] T. Chen, G. Zhang, H. Sun, Y. Hua, S. Yang, D. Zhou, H. Di, Y. Xiong, S. Hou, H. Xu, L. Zhang, Robust Fe-N_4-C_6O_2 single atom sites for efficient PMS activation and enhanced Fe^{IV} = O reactivity, Nat. Commun. 16 (2025) 2402, https://doi.org/10.1038/s41467-025-57643-7.
[26] M.M. El-Zahed, M.A. Diab, A.Z. El-Sonbati, M.H. Saad, A.M. Eldesoky, M.A. El-Bindary, Synthesis, spectroscopic characterization studies of chelating complexes and their applications as antimicrobial agents, DNA binding, molecular docking, and electrochemical studies, Appl. Organomet. Chem. 38 (2024) e7290, https://doi.org/10.1002/aoc.7290.
[27] V.K. Juyal, A. Pathak, M. Panwar, S.C. Thakuri, O. Prakash, A. Agrwal, V. Nand, Schiff base metal complexes as a versatile catalyst: a review, J. Organomet. Chem. 999 (2023) 122825, https://doi.org/10.1016/j.jorganchem.2023.122825.
[28] C. Li, R. Wang, W. Sun, K. Cui, X. Fu, M. Cui, Y. Chen, Z. Guo, Y. Liu, Efficient degradation of Rhodamine B by visible-light-driven biomimetic Fe(III) complex/peroxymonosulfate system: The key role of FeV=O, J. Environ. Chem. Eng. 12 (2024) 113288, https://doi.org/10.1016/j.jece.2024.113288.
[29] D. Zhao, K. Yu, P. Song, W. Feng, B. Hu, W. Cheong, Z. Zhuang, S. Liu, K. Sun, J. Zhang, C. Chen, Atomic-level engineering $Fe_1N_2O_2$ interfacial structure derived from oxygen-abundant metal–organic frameworks to promote electrochemical CO_2 reduction, Energy & Environ. Sci. 15 (2022) 3795–3804, https://doi.org/10.1039/D2EE00878E.
[30] Y. Wang, R. Shi, L. Shang, G.I.N. Waterhouse, J. Zhao, Q. Zhang, L. Gu, T. Zhang, High-efficiency oxygen reduction to hydrogen peroxide catalyzed by nickel single-atom catalysts with tetradentate N_2O_2 coordination in a three-phase flow cell, Angew. Chem. Int. Ed. 59 (2020) 13057–13062, https://doi.org/10.1002/anie.202004841.
[31] M.A. Malik, O.A. Dar, P. Gull, M.Y. Wani, A.A. Hashmi, Heterocyclic Schiff base transition metal complexes in antimicrobial and anticancer chemotherapy, RSC Med. Chem. 9 (2018) 409–436, https://doi.org/10.1039/C7MD00526A.
[32] M.J. Frisch, et al., Gaussian 16, Revision C.01, Gaussian, Inc, Wallingford CT, 2016.
[33] A.L. Cazetta, T. Zhang, T.L. Silva, V.C. Almeida, T. Asefa, Bone char-derived metal-free N- and S-co-doped nanoporous carbon and its efficient electrocatalytic activity for hydrazine oxidation, Appl. Catal. B Environ. 225 (2018) 30–39, https://doi.org/10.1016/j.apcatb.2017.11.050.
[34] Q. Xu, Q. Lv, C. Zhao, W. Du, Z. Liu, Z. Guo, Single-atom transition metal (Fe, Co, and Ni) site-anchored N-doped carbon spheres for highly sensitive detection of carbendazim, Sens. Actuators B Chem. 462 (2026) 140027, https://doi.org/10.1016/j.snb.2026.140027.
[35] L. Liu, B. Chen, T. Wu, M. Li, H. Chen, Y. Ge, Z. Li, Coordination Reconstruction Enhanced Synergistic Nonradical Oxidation Pathways in Cobalt Single-Atom Catalysts for Sustained Pollutant Destruction, Angew. Chem. Int. Ed. 64 (2025) e202508330, https://doi.org/10.1002/anie.202508330.
[36] A. Sadezky, H. Muckenhuber, H. Grothe, R. Niessner, U. Pöschl, Raman microspectroscopy of soot and related carbonaceous materials: Spectral analysis and structural information, Carbon 43 (2005) 1731–1742, https://doi.org/10.1016/j.carbon.2005.02.018.
[37] D. Yuan, C. Zhang, S. Tang, M. Sun, Y. Zhang, Y. Rao, Z. Wang, J. Ke, Fe^{3+}-sulfite complexation enhanced persulfate Fenton-like process for antibiotic degradation based on response surface optimization, Sci. Total. Environ. 727 (2020) 138773, https://doi.org/10.1016/j.scitotenv.2020.138773.
[38] S. Zhang, B. Sun, K. Liao, X. Wang, Z. Chen, J. Wang, W. Hu, X. Han, Boosting Oxygen Reduction Reaction Performance of Fe Single-Atom Catalysts Via Precise Control of the Coordination Environment, Adv. Funct. Mater. 35 (2025) 2425640, https://doi.org/10.1002/adfm.202425640.
[39] H. Shi, H. Zhang, T. Wang, S. Chen, Regulating the electronic structure of iron sites in single-atom catalyst with interfacial chemical bond to enhance Fenton-like reaction, J. Hazard. Mater. 488 (2025) 137483, https://doi.org/10.1016/j.jhazmat.2025.137483.
[40] Z. Wang, W. Wang, J. Wang, Y. Yuan, Q. Wu, H. Hu, High-valent iron-oxo species mediated cyclic oxidation through single-atom Fe-N_6 sites with high peroxymonosulfate utilization rate, Appl. Catal. B Environ. 305 (2022) 121049, https://doi.org/10.1016/j.apcatb.2021.121049.
[41] X. Wang, Z. Xiong, S. Yang, H. Zhou, Y. Shi, Z. Wu, B. Huang, L. Yang, C. He, X. Duan, B. Lai, Proximity Engineering of Fe-N_4 Twins for Oriented Generation of Singlet Oxygen for Hospital Wastewater Treatment, Angew. Chem. Int. Ed. 65 (2026) e6249880, https://doi.org/10.1002/anie.6249880.
[42] J. Hu, W. Shang, C. Xin, J. Guo, X. Cheng, S. Zhang, S. Song, W. Liu, F. Ju, J. Hou, Y. Shi, Uncovering Dynamic Edge-Sites in Atomic Co−N−C Electrocatalyst for Selective Hydrogen Peroxide Production, Angew. Chem. Int. Ed. 62 (2023) e202304754, https://doi.org/10.1002/anie.202304754.
[43] J.Q. Zhang, J. Ma, J. Zou, H.Z. Chi, Y. Song, Spectrophotometric determination of peroxymonosulfate anions via oxidative decolorization of dyes induced by cobalt, Anal. Methods 8 (2016) 973–978, https://doi.org/10.1039/C5AY02886H.
[44] L. Peng, X. Duan, Y. Shang, B. Gao, X. Xu, Engineered carbon supported single iron atom sites and iron clusters from Fe-rich Enteromorpha for Fenton-like reactions via nonradical pathways, Appl. Catal. B Environ. 287 (2021) 119963, https://doi.org/10.1016/j.apcatb.2021.119963.
[45] C. Zhu, Y. Nie, F. Cun, Y. Wang, Z. Tian, F. Liu, Two-step pyrolysis to anchor ultrahigh-density single-atom FeN_5 sites on carbon nitride for efficient Fenton-like catalysis near 0 °C, Appl. Catal. B Environ. 319 (2022) 121900, https://doi.org/10.1016/j.apcatb.2022.121900.
[46] L. Jiang, Z. Hu, S. Xie, Z. Shangguan, Q. Lu, H. Chen, J. Guo, J. Li, W. Zhao, H. Wang, X. Yuan, Z. Liu, Axial oxygen-coordinated asymmetric structure Fe-N_4O_1 enhanced non-radical pathway for ultrafast degradation, Appl. Catal. B Environ. Energy 394 (2026) 126810, https://doi.org/10.1016/j.apcatb.2026.126810.
[47] H. Liu, J. Liang, X. Du, R. Wang, T. Tang, X. Tao, H. Yin, Z. Dang, G. Lu, Degradation of tris(2-chloroethyl) phosphate (TCEP) by thermally activated persulfate: Combination of experimental and theoretical study, Sci. Total. Environ. 809 (2022) 152185, https://doi.org/10.1016/j.scitotenv.2021.152185.
[48] X. Li, Y. Fang, W. Xu, R. Hu, X. Li, P. Tan, J. Yu, Conversion of peroxymonosulfate to singlet oxygen by single-atom catalysts for water remediation, Sep. Purif. Technol. 328 (2024) 125036, https://doi.org/10.1016/j.seppur.2023.125036.
[49] P. Duan, M. Li, X. Xu, Q. Yue, Y. Gao, B. Gao, Understanding of interfacial molecular interactions and inner-sphere reaction mechanism in heterogeneous

Fenton-like catalysis on Mn-N_4 site, Appl. Catal. B Environ. Energy 344 (2024) 123619, https://doi.org/10.1016/j.apcatb.2023.123619.
[50] Y. Zhou, J. Jiang, Y. Gao, S. Pang, Y. Yang, J. Ma, J. Gu, J. Li, Z. Wang, L. Wang, L. Yuan, Y. Yang, Activation of peroxymonosulfate by phenols: Important role of quinone intermediates and involvement of singlet oxygen, Water Res. 125 (2017) 209–218, https://doi.org/10.1016/j.watres.2017.08.049.
[51] J. Al-Nu'airat, B.Z. Dlugogorski, X. Gao, N. Zeinali, J. Skut, P.R. Westmoreland, I. Oluwoye, M. Altarawneh, Reaction of phenol with singlet oxygen, Phys. Chem. Chem. Phys. 21 (2019) 171–183, https://doi.org/10.1039/C8CP04852E.
[52] Z. Chen, F. An, Y. Zhang, Z. Liang, W. Liu, M. Xing, Single-atom Mo–Co catalyst with low biotoxicity for sustainable degradation of high-ionization-potential organic pollutants, Proc. Natl. Acad. Sci. 120 (2023) e2305933120, https://doi.org/10.1073/pnas.2305933120.
[53] X. Li, X. Wen, J. Lang, Y. Wei, J. Miao, X. Zhang, B. Zhou, M. Long, P.J.J. Alvarez, L. Zhang, CoN_1O_2 Single-Atom Catalyst for Efficient Peroxymonosulfate Activation and Selective Cobalt(IV)=O Generation, Angew. Chem. Int. Ed. 62 (2023) e202303267, https://doi.org/10.1002/anie.202303267.
[54] W. Ren, C. Cheng, P. Shao, X. Luo, H. Zhang, S. Wang, X. Duan, Origins of Electron-Transfer Regime in Persulfate-Based Nonradical Oxidation Processes, Environ. Sci. & Technol. 56 (2022) 78–97, https://doi.org/10.1021/acs.est.1c05374.
[55] Z. Zhu, Y. Wang, P. Wang, S. Zhong, K. Hu, S. Ren, J.P. Vongsvivut, H. Sun, X. Duan, S. Wang, Multidimensional engineering of single-atom cobalt catalysts for ultrafast Fenton-like reactions, Nat. Water 3 (2025) 211–221, https://doi.org/10.1038/s44221-024-00382-8.
[56] F. Chen, L. Liu, J. Wu, X. Rui, J. Chen, Y. Yu, Single-Atom Iron Anchored Tubular g-C_3N_4 Catalysts for Ultrafast Fenton-Like Reaction: Roles of High-Valency Iron-Oxo Species and Organic Radicals, Adv. Mater. 34 (2022) 2202891, https://doi.org/10.1002/adma.202202891.
[57] J. He, Y. Wan, W. Zhou, ZIF-8 derived Fe-N coordination moieties anchored carbon nanocubes for efficient peroxymonosulfate activation via non-radical pathways: Role of FeN_x sites, J. Hazard. Mater. 405 (2021) 124199, https://doi.org/10.1016/j.jhazmat.2020.124199.
[58] H. Liu, X. Shu, M. Huang, B. Wu, J. Chen, X. Wang, H. Li, H. Yu, Tailoring d-band center of high-valent metal-oxo species for pollutant removal via complete polymerization, Nat. Commun. 15 (2024) 2327, https://doi.org/10.1038/s41467-024-46739-1.
[59] Z. Zhao, H. Dai, T. Nie, T. Hu, W. Zhou, M. Zhang, J. Xu, D. Lin, L. Zhu, Dynamic electronic modulation of single-atom Fe sites with p-block metal coordination enables highly selective generation of FeIV = O in Fenton-like reactions, Nat. Commun. 16 (2025) 11290, https://doi.org/10.1038/s41467-025-66177-x.
[60] Z. Wu, B. Huang, X. Wang, C. He, Y. Liu, Y. Du, W. Liu, Z. Xiong, B. Lai, Facilely Tuning the First-Shell Coordination Microenvironment in Iron Single-Atom for Fenton-like Chemistry toward Highly Efficient Wastewater Purification, Environ. Sci. & Technol. 57 (2023) 14046–14057, https://doi.org/10.1021/acs.est.3c04343.
[61] F. Huang, X. Long, T. Li, X. Guo, L. Hu, H. Zhao, S. Tian, M. Su, C. He, Manipulating non-radical pathway preference in PMS-mediated phenolic degradation: Substituent-dependent catalyst-pollutant interfacial interaction over single-atom Fe-N-C, Chem. Eng. J. 535 (2026) 175428, https://doi.org/10.1016/j.cej.2026.175428.
[62] J. Lu, A. Ding, L. Wang, W. Zhao, K. Zhang, M. Liu, X. Liu, Y. Li, Z. Li, D. Wu, Spin States of Fe-N_4 Sites Regulates PMS Activation Pathways for Ultrafast Sulfamethoxazole Degradation, Small 22 (2026) e14930, https://doi.org/10.1002/smll.202514930.
[63] R. Malik, N. Stolte, H. Forbert, A. Chandra, D. Marx, Accurate Determination of Isotope Effects on the Dynamics of H-Bond Breaking and Making in Liquid Water, J. Phys. Chem. Lett. 16 (2025) 3727–3733, https://doi.org/10.1021/acs.jpclett.5c00210.
[64] J. Fan, H. Qin, S. Jiang, Mn-doped g-C_3N_4 composite to activate peroxymonosulfate for acetaminophen degradation: the role of superoxide anion and singlet oxygen, Chem. Eng. J. 359 (2019) 723–732, https://doi.org/10.1016/j.cej.2018.11.165.
[65] M. Yan, Y. Li, Q. Xu, X. Wei, P. Xiao, F. Chen, L. Yang, X. Wu, Enhanced electron-transfer for peroxymonosulfate activation by Ni single sites adjacent to Ni nanoparticles, J. Colloid Interface Sci. 654 (2024) 979–987, https://doi.org/10.1016/j.jcis.2023.10.096.
[66] Q. Tang, B. Wu, X. Huang, W. Ren, L. Liu, L. Tian, Y. Chen, L. Zhang, Q. Sun, Z. Kang, T. Ma, J. Zou, Electron transfer mediated activation of periodate by contaminants to generate $^1O_2$ by charge-confined single-atom catalyst, Nat. Commun. 15 (2024) 9549, https://doi.org/10.1038/s41467-024-53941-8.
[67] P. Li, H. Wang, X. Tan, W. Hu, M. Huang, J. Shi, J. Chen, S. Liu, Z. Shi, Z. Li, Bifunctional electrocatalyst with CoN_3 active sties dispersed on N-doped graphitic carbon nanosheets for ultrastable Zn-air batteries, Appl. Catal. B Environ. 316 (2022) 121674, https://doi.org/10.1016/j.apcatb.2022.121674.
[68] Q. Tian, Y. Liu, Q. Li, X. Zhao, Y. Li, N. Li, Y. Wang, Y. Shi, X. Xu, Atomic coordination engineering and pollutants synergy co-modulate self-motivated single-atom catalysis with zero-oxidant addition for sustainable water purification, Sci. Bull. 71 (2026) 2552–2563, https://doi.org/10.1016/j.scib.2026.04.017.
[69] C. Cheng, W. Ren, F. Miao, X. Chen, X. Chen, H. Zhang, Generation of Fe^{IV}=O and its contribution to Fenton-like reactions on a single-atom iron−N−C catalyst, Angew. Chem. Int. Ed. 62 (2023) e202218510, https://doi.org/10.1002/anie.202218510.
[70] P. Zhang, C. Zhao, F. Jiang, C. Wu, T. Wang, X. Xu, M. Wu, Z. Chen, Y. Zou, Atomically engineered Fe/Mn catalysts enable ultrafast self-sustaining water purification via oxidant-free Fenton-like electron-transfer reaction, Water Res. 297 (2026) 125752, https://doi.org/10.1016/j.watres.2026.125752.
[71] F. Xu, C. Lai, M. Zhang, B. Li, L. Li, S. Liu, D. Ma, X. Zhou, H. Yan, X. Huo, B. Wang, H. Yi, L. Qin, L. Tang, High-loaded single-atom Cu-N_3 sites catalyze hydrogen peroxide decomposition to selectively induce singlet oxygen production for wastewater purification, Appl. Catal. B Environ. 339 (2023) 123075, https://doi.org/10.1016/j.apcatb.2023.123075.
[72] X. Wei, S. Song, W. Cai, X. Luo, L. Jiao, Q. Fang, X. Wang, N. Wu, Z. Luo, H. Wang, Z. Zhu, J. Li, L. Zheng, W. Gu, W. Song, S. Guo, C. Zhu, Tuning the spin state of Fe single atoms by Pd nanoclusters enables robust oxygen reduction with dissociative pathway, Chem 9 (2023) 181–197, https://doi.org/10.1016/j.chempr.2022.10.001.
[73] Y. Bai, G. Zhang, M. Liu, S. Hou, S. Zheng, S. Yang, C. Zhu, H. Xu, Spatial axial oxygen coordination of CoSA-N_2O_1/MXene single-atom catalyst with electron-depleted active site for selective $^1O_2$ generation, Appl. Catal. B Environ. Energy 374 (2025) 125378, https://doi.org/10.1016/j.apcatb.2025.125378.
[74] K. Yin, Y. Shang, D. Chen, B. Gao, Q. Yue, X. Xu, Redox potentials of pollutants determining the dominate oxidation pathways in manganese single-atom catalyst (Mn-SAC)/peroxymonosulfate system: selective catalytic mechanisms for versatile pollutants, Appl. Catal. B Environ. 338 (2023) 123029, https://doi.org/10.1016/j.apcatb.2023.123029.
[75] Y. Jiang, K. Gao, T. Chen, Y. Xiong, Y. Li, A. Addisu, S.C. Pillai, D.D. Dionysiou, D. Wang, Regulating the generation of singlet oxygen ($^1O_2$) in Advanced oxidation processes by catalyst design for water treatment, Chem. Eng. J. 500 (2024) 156532, https://doi.org/10.1016/j.cej.2024.156532.
[76] Y. Liu, C. Zhang, X. Wang, Y. Gao, X. Zhang, G. Wang, High-efficiency and sustainable peroxymonosulfate activation on Fe single-atom catalyst through incorporating complementary S species for enhanced water decontamination, J. Colloid Interface Sci. 692 (2025) 137533, https://doi.org/10.1016/j.jcis.2025.137533.